

1 **TITLE**

2 **Optical flow analysis reveals that Kinesin-mediated advection impacts on the orientation of**  
3 **microtubules in the *Drosophila* oocyte**

4

5 **RUNNING TITLE**

6 Microtubule orientation analyzed by optical flows

7

8 **AUTHORS**

9 Maik Drechsler<sup>a,b,c,†,\*</sup>, Lukas F. Lang<sup>d,†</sup>, Layla Al-Khatib<sup>a</sup>, Hendrik Dirks<sup>e</sup>, Martin Burger<sup>f</sup>, Carola-  
10 Bibiane Schönlieb<sup>d</sup> and Isabel M. Palacios<sup>a,b,\*</sup>

11

12 **AUTHOR AFFILIATIONS**

13 <sup>a</sup>*School of Biological and Chemical Sciences, Queen Mary University of London, Mile End Road, London E1 4NS, UK*

14 <sup>b</sup>*Department of Zoology, University of Cambridge, Cambridge CB2 3EJ, UK*

15 <sup>c</sup>*Department of Zoology and Developmental Biology, University of Osnabrück, Barbarastraße 11, 49076 Osnabrück,*  
16 *Germany*

17 <sup>d</sup>*Department of Applied Mathematics and Theoretical Physics, University of Cambridge, Wilberforce Road, Cambridge*  
18 *CB3 0WA, UK*

19 <sup>e</sup>*Institute for Computational and Applied Mathematics, University of Münster, Einsteinstraße 62, 48149 Münster,*  
20 *Germany*

21 <sup>f</sup>*Department of Mathematics, Friedrich-Alexander Universität Erlangen-Nürnberg, Cauerstraße 11, 91058 Erlangen,*  
22 *Germany*

23

24 <sup>\*</sup>*Corresponding authors:*

25 [madrechs@uos.de](mailto:madrechs@uos.de) tel. +49 (0)541 969 2849

26 [i.palacios@qmul.ac.uk](mailto:i.palacios@qmul.ac.uk) tel. +44 (0)20 7882 6909

27 <sup>†</sup>equal contribution

28

29 **KEY WORDS**

30 *self-organization; active processes; optical flow; cytoplasmic streaming; cytoplasmic flows;*  
31 *microtubules; plus ends; motor proteins*

32 **ABSTRACT**

33 The orientation of microtubule networks is exploited by motors to deliver cargoes to specific  
34 intracellular destinations, and is thus essential for cell polarity and function. Reconstituted *in vitro*  
35 systems have largely contributed to understanding the molecular framework regulating the  
36 behavior of microtubule filaments. In cells however, microtubules are exposed to various  
37 biomechanical forces that might impact on their orientation, but little is known about it. Oocytes,  
38 which display forceful cytoplasmic streaming, are excellent model systems to study the impact of  
39 motion forces on cytoskeletons *in vivo*. Here we implement variational optical flow analysis as a  
40 new approach to analyze the polarity of microtubules in the *Drosophila* oocyte, a cell that displays  
41 distinct Kinesin-dependent streaming. After validating the method as robust for describing  
42 microtubule orientation from confocal movies, we find that increasing the speed of flows results in  
43 aberrant plus end growth direction. Furthermore, we find that in oocytes where Kinesin is unable to  
44 induce cytoplasmic streaming, the growth direction of microtubule plus ends is also altered. These  
45 findings lead us to propose that cytoplasmic streaming - and thus motion by advection -  
46 contributes to the correct orientation of MTs *in vivo*. Finally, we propose a possible mechanism for  
47 a specialised cytoplasmic actin network (the actin mesh) to act as a regulator of flow speeds; to  
48 counteract the recruitment of Kinesin to microtubules.

49

50 **HIGHLIGHT SUMMARY**

51 Cytoskeletal networks do not exist in isolation, but experience crowded and dynamic intracellular  
52 environments. However, microtubule-environment interactions are not well understood, and such  
53 system-environment interactions are an unresolved question in biology that demands bridging  
54 across disciplines. Here we introduce an optical flow motion estimation approach to study  
55 microtubule orientation in the *Drosophila* oocyte, a cell displaying substantial cytoplasmic  
56 streaming. We show that microtubule polarity is affected by the regime of these flows, and  
57 furthermore, that the presence of flows is necessary for MTs to adopt their proper polarity. With  
58 these findings we are contributing to further understanding how microtubules organize in their  
59 impacting natural environment.

## 60 INTRODUCTION

61 Eukaryotic life depends on many dynamic processes, including for example cell division, cell  
62 migration, and cell polarization. These processes in turn strongly rely on highly organized  
63 microtubule (MT) arrays. All MT networks are polarized, with the minus end of each filament linked  
64 to a nucleating centre (MT organising centre or MTOC), and the plus end growing away from these  
65 centres. This polarity is exploited by specific motor proteins to transport cargoes along MTs in a  
66 defined direction, and is thus essential for the function of MT networks.

67 A number of biophysical studies, using reconstituted *in vitro* systems, have helped to understand  
68 the mechanical properties of MTs, setting the stage for deciphering the behavior of MTs *in vivo*.  
69 However, much needs to be learnt about the properties of MTs in their natural intracellular  
70 environment. For example, a rather new concept emanating from *in vivo* experiments is that  
71 controlling nucleation and the position of minus ends of single filaments alone is not always  
72 sufficient to establish the proper polarity of the entire MT network. MT plus ends must be controlled  
73 as well in order to allow motor proteins to deliver their cargoes to the correct destination. Plus ends  
74 can be regulated at various levels, including dynamic instability, capturing, and direction of growth.  
75 Dynamic instability describes a process in which MT polymerisation is interrupted by a rapid  
76 depolymerisation phase, followed by a 'rescue' process (Mitchison and Kirschner, 1984). Various  
77 MT-associated proteins, such as motors and MT plus end-tracking proteins (+TIPs), are known to  
78 regulate dynamic instability (Akhmanova and Steinmetz, 2015). MT plus ends can also be  
79 captured at the cell cortex, a process also involving +TIPs and motors, such as the  
80 Dynein/Dynactin complex (Nieuwburg *et al.*, 2017) (and reviewed in (Akhmanova and Steinmetz,  
81 2015)). However, very little is known about how the direction of growth of plus ends, and therefore  
82 the orientation of MTs, is controlled in cells. In axons, adenomatous polyposis coli (APC) seems to  
83 regulate plus end direction (Purro *et al.*, 2008), while Fidgetin-like1, a MT-associated ATPase,  
84 controls both dynamics and plus ends direction (Fassier *et al.*, 2018). MT bending also impacts on  
85 the direction of plus tip growth, as the MT tip rotates due to local bend formation (Kent *et al.*,  
86 2016). Furthermore, +TIPs that contain actin-binding motifs can influence MT growth direction by  
87 guiding dynamic plus ends along actin bundles (Kodama *et al.*, 2003; Jiang *et al.*, 2012).

88 In the mid-oogenesis stage 9 (st9) oocyte of *Drosophila melanogaster*, MTs are nucleated from the  
89 antero-lateral cortex in a gradient of diminishing abundance toward the posterior pole, where  
90 nucleation is absent. In addition, the growing plus ends exhibit a weak posterior orientation bias  
91 (Doerflinger *et al.*, 2006; Parton *et al.*, 2011; Nashchekin *et al.*, 2016). This weak polarization bias  
92 of plus ends towards the posterior pole of the oocyte is sufficient and necessary for the localization  
93 of body plan determinants to the very 'posterior tip', as well as the formation of the pole plasm  
94 (needed for germ cell development) in this region. For example, the plus end motor Kinesin-1 (Kin  
95 from here on) localizes *oskar* mRNA to the 'posterior tip' of the st9 oocyte, an essential step in the  
96 establishment of the anterior-posterior (A-P) axis and the formation of the pole plasm (Brendza *et*  
97 *al.*, 2000).

98 In addition to a polarized MT cytoskeleton, the oocyte displays a Kin-dependent bulk motion of the  
99 cytoplasm called cytoplasmic streaming or flows (Palacios and St Johnston, 2002; Serbus *et al.*,  
100 2005; Ganguly *et al.*, 2012; Drechsler *et al.*, 2017). Compared to st9, late stage oocytes (st11)  
101 exhibit faster and larger scale flows that are induced not only by Kin-mediated viscous drag of  
102 transported cargo (similar to st9), but also by Kin-mediated MT-sliding (Lu *et al.*, 2016; Monteith *et*  
103 *al.*, 2016). At these later developmental stages, these faster flows are important for mixing the  
104 cytoplasm of the large oocyte (Ganguly *et al.*, 2012), and aiding the asymmetric localization of  
105 developmental determinants and mitochondria (Forrest and Gavis, 2003; Hurd *et al.*, 2016; Lu *et*  
106 *al.*, 2018). In addition, mathematical modeling has suggested that faster flows can induce parallel  
107 MT arrays when the MTs are near a barrier (such as the cortex)(Monteith *et al.*, 2016). However, in  
108 st9 oocytes, when posterior cargoes such as *oskar* mRNA are first localized, MT sliding has been  
109 excluded as the source of cytoplasmic streaming (Lu *et al.*, 2016). Cytoplasmic flows at st9 are  
110 slowed down by a cytoplasmic actin mesh. When this actin mesh dissolves during mid-oogenesis,  
111 the flows become faster and more organized, and the MT arrange into sub-cortical bundles  
112 (Dahlgard *et al.*, 2007; Quinlan, 2013). However, the mechanism by which the actin mesh  
113 regulates flows is unknown. Furthermore, it is unclear whether cytoplasmic flows at st9 have an  
114 impact on the organization of the MT cytoskeleton. Recently, we found that st9 flows constitute a  
115 key force driving the persistent motion of vesicles and actin filaments (Drechsler *et al.*, 2017).  
116 These observations prompted us to address the question of how advection (active transport  
117 induced by fluid flows) impacts on the polarization of the MT network in st9 oocytes. In this way,  
118 we aim to contribute to the insufficient knowledge on how the direction of MT growth is controlled  
119 *in vivo*.

120 In order to assess the global MT orientation in st9 oocytes, and to investigate the growth direction  
121 of MT plus ends *in vivo*, we used EB1::GFP (EB1 from here on). EB1 exclusively decorates the  
122 growing plus end of MTs, resulting in dynamic 'comets' moving through the cytoplasm at a speed  
123 of ~100-600 nm/sec across various cell types, including the oocyte (at an average and maximum  
124 speeds of 230 nm/sec and 600 nm/s, respectively (Parton *et al.*, 2011; Nieuwburg *et al.*, 2017).  
125 Analyzing the orientation of MTs in complex networks has proven technically challenging, and  
126 requires suitable imaging and image analysis tools. Especially for the *Drosophila* oocyte, we found  
127 the published method too demanding on the imaging level, requiring state of the art wide-field  
128 deconvolution microscopy and elaborate image processing (Parton *et al.*, 2011), and thus  
129 unfeasible for the various experimental conditions that our study required. Here, we developed an  
130 image analysis strategy that allows an efficient characterisation of direction and distribution of EB1  
131 comets from confocal image series by an optical flow (OF)-based motion estimation approach. In  
132 general, OF allows to estimate the apparent motion of objects or other intensity variations in a  
133 sequence of images (Horn and Schunck, 1981). In addition, variational OF methods constitute a  
134 well-established framework for dense motion estimation, and do not require elaborate  
135 segmentation or tracking of the studied structures. OF methods outperform popular methods, such

136 as particle image velocimetry (PIV), for motion analysis in certain settings and, in particular, in the  
137 presence of noise (Ruhnau et al., 2005; Vig et al., 2016). While variational OF methods have been  
138 used predominantly to investigate the dynamics of entire cells (Amat et al., 2013; Boric et al., 2013;  
139 Guo, 2014), recent works focused also on intracellular motility (Delpiano et al., 2012; Frerking et  
140 al., 2014; Vig et al., 2016; Boquet-Pujadas et al., 2017; Huang et al., 2017).

141 In this study, we investigated how cytoplasmic streaming influences the polarization of the MT  
142 cytoskeleton. For this, we introduce a two-step image analysis approach that is based on image  
143 denoising and variational OF, and is able to estimate approximate velocities (speed and direction)  
144 of EB1 motion in confocal image sequences. This approach will assist many researchers  
145 interested in characterizing MT polarity from confocal images of their tissue of choice. Our findings  
146 revealed that cytoplasmic streaming is necessary and sufficient to regulate the polarity of the MT  
147 network in st9 oocytes. Furthermore, our data suggests that the actin mesh regulates the  
148 recruitment of Kin to MTs, indicating a new mechanism by which the actin cytoskeleton influences  
149 MT-based transport and advection. With this work, we further contribute to understanding the *in*  
150 *vivo* properties of MTs, and the interactions of MTs with their natural environment.

## 151 RESULTS

152

### 153 Quantification of MT plus-tip directionality by optical flow analysis

154 To study the spatial orientation of MT filaments *in vivo*, we used oocytes expressing EB1 (Figures  
155 1, 3, 4 and 5). EB1 constitutes a marker for growing MT plus-tips and has been used in fly oocytes  
156 before (Parton *et al.*, 2011; Nieuwburg *et al.*, 2017). In these previous studies, wide-field  
157 deconvolution microscopy was used to image EB1 dynamics in various areas of st9 oocytes.  
158 However, wide-field microscopy has a limited focus depth, only allowing to image EB1 dynamics  
159 close to the cortex of the relatively large oocyte, and requires a complex acquisition procedure. In  
160 order to improve imaging depth and simplify the acquisition procedure, we implemented a strategy  
161 that combines conventional confocal microscopy with image denoising and motion analysis by  
162 variational OF analysis.

163 OF-based motion estimation relies on the assumption that particles approximately maintain their  
164 pixel intensity as they move. In thick biological samples the intensity of fluorescent signals declines  
165 with the depth of the imaging plane. To minimize the effects of tissue thickness on signal intensity,  
166 we imaged within a single focal plane in the middle of the oocyte over the course of at least one  
167 minute (for details see Material and Methods). With this approach, we avoided measurable  
168 bleaching and ensured that EB1 comets would only be detected within a thin focal plane of  $\sim 1.3$   
169  $\mu\text{m}$ . Thus, comets moving orthogonally to the focal plane would be lost instead of getting dimmer  
170 or brighter. As a consequence, our analyzes capture the 2D motion of EB1 comets within a 3D  
171 intracellular environment. However, the orientation of individual oocytes on the microscope slide is  
172 random. Together with averaging across several cells, this results in 2D data obtained from various  
173 angles (one precise orientation per cell), which indirectly allows to acquire information about the  
174 3D behavior. As OF is formulated on a per-pixel basis, this method allows inferring a displacement  
175 vector for each pixel and does not require sophisticated tracking of individual particles (Figure 1A  
176 and B). Since MTs grow one order of magnitude faster compared to the speed of cytoplasmic flows  
177 in st9 oocytes, we took one image every 650 ms, resulting in a loss of spatial resolution, and  
178 causing the raw data to exhibit considerable high noise (Figure 1D). Due to this high noise level,  
179 preceding denoising of the image data was required prior to applying the motion estimation. We  
180 found that total variation-based (Rudin *et al.*, 1992) image denoising with additional temporal  
181 regularization was sufficient to improve the signal-to-noise ratio and the visibility of EB1 comets  
182 (Figure 1E, Figure S1-S3 and Movie S1).

183 In the next step, displacement vector fields were computed with a variational OF method (Figure  
184 S4). After accounting for the pixel size and the time interval between consecutive frames, these  
185 displacements can be regarded as approximate velocities of EB1 motion (Figure 1F-H).  
186 Importantly, the acquired velocities are a sum of all motion experienced by the imaged EB1 signal,  
187 including filament growth and MT displacement by advection and transport. A typical image  
188 sequence of 100 frames and a 512 x 256 pixel resolution results in a total number of approximately

189 13 million computed vectors that require appropriate interpretation. The computation time for  
190 processing one typical sequence amounted to less than 25 minutes on average.

191 We visualized the estimated vector fields with the help of a standard colour-coding (Baker, 2011).  
192 The vector at each pixel and at a certain frame is represented by a colour that is determined by the  
193 direction of the signal's movement (see the colour-coding at the boundary of the images in Figure  
194 1F-H). The colour's intensity is determined by the relative velocity of the signal. The stronger the  
195 intensity, the higher the velocity. For our statistical analyzes, we considered only vectors located  
196 within a hand-drawn segmentation mask that outlines the oocyte in each sequence (Figure 1H).  
197 The direction of each vector could then be represented in polar coordinates. The distribution of the  
198 angles obtained from each individual cell is visualized in a rose diagram (Figure 1O and P). In  
199 addition, we show the histogram of the distributions averaged over all cells of a given genotype  
200 (Figure 1Q).

201 We then used OF to describe the MT orientation in control oocytes (Figure 1O-S, Figure S5). Since  
202 all cells were orientated with the posterior pole to the right during imaging, the angles given in the  
203 rose diagram reflect the directional movement of EB1 comets. For a quantitative description of MT  
204 orientation, we determined the mean angular direction of the estimated motion of EB1 signals ( $\theta_{avg}$ ,  
205 considering all recorded cells of one genotype, Figure 1R, Table 1) and the frequency of  
206 movements directed towards the anterior (all within the region  $270^\circ$  to  $90^\circ$ , blue semicircle in  
207 Figure 1C) or the posterior (all within the region  $90^\circ$  to  $270^\circ$ , orange semicircle in Figure 1C). As a  
208 descriptor of how focused MTs grow towards the very 'posterior tip', we also determined the  
209 relative frequency of posterior-directed EB1 signals that fall within a sector of  $60^\circ$  (from  $30^\circ$  to  
210  $330^\circ$ ), called 'posterior tip', inspired by the region where determinants localize and pole plasm  
211 forms (light orange sector in Figure 1C). This 'posterior tip' frequency only considers EB1 signals  
212 that were previously found to grow towards the posterior (orange semicircle in Figure 1C), and  
213 thus the 'posterior tip' value represents a sub-population of all posterior signals that grow with an  
214 angle between  $30^\circ$  to  $330^\circ$ . In summary, we find that all growing MTs exhibit a global (over the  
215 entire oocyte) posterior orientation bias, with 66% of all comets growing towards the posterior of  
216 control cells (Figure 1R). These findings are in agreement with previous reports of biased MT  
217 orientation in st9 oocytes (Parton et al., 2011), and provide a first level of validation to establish OF  
218 as a reliable way to investigate the orientation of MTs. In addition, we find that 40% of the 66% of  
219 comets that grow towards the posterior are oriented towards the 'posterior tip', where determinants  
220 localize and the pole plasm forms (Figure 1S).

221

## 222 **OF is sufficient to detect changes in microtubule network orientation**

223 In order to test whether OF-based approaches are able to capture EB1 directionality in other cell  
224 types, we investigated EB1 comets in the follicular epithelium surrounding the egg chamber. In  
225 these epithelial cells, MTs are nucleated apically and grow predominantly towards the basal

226 membrane, parallel to the lateral membranes of the cell. Notably, single comets can easily be  
227 identified and followed by eye, which allowed us to assess the accuracy of the OF results. OF  
228 analysis captures the directionality of MTs in these follicle cells accurately, supporting the  
229 suitability of the approach to estimate MT orientation *in vivo* (Movie S2 and Figure S6-S7).

230 We next tested whether OF can pick up changes in the architecture of MT networks in the oocyte,  
231 and analyzed cells harboring a mutation in *gurken* (*grk*), which exhibit MT organization and cell  
232 polarity defects (Gonzalez-Reyes *et al.*, 1995; Roth *et al.*, 1995; Januschke *et al.*, 2002). With our  
233 OF analysis we were able to detect an aberrant MT organization in *grk* oocytes, with EB1 comets  
234 showing a variable orientation from cell-to-cell (Movie S3 and Figure S6). Although, the number of  
235 tested cells is low, and thus the actual biological meaning of these findings needs further  
236 investigation, our results confirm that OF is able to detect aberrations in MT networks in complex  
237 systems like the oocyte.

238

### 239 **Aberrantly fast cytoplasmic flows change MT motion, bundling and orientation**

240 In order to investigate the relationship between cytoplasmic advection and the organization of the  
241 MT network, we monitored the bulk behavior of MTs in control cells and in oocytes with faster  
242 flows. Oocytes mutant for *cappuccino* (*capu*) or *spire* display faster flows at st9 (Figure S9A, B)  
243 and fail to localize posterior cargoes like the mRNA-binding protein Staufen (Figure 1I, K and M)  
244 (Theurkauf, 1994; Dahlgard *et al.*, 2007; Quinlan, 2013). Capu (a formin) and Spire are actin  
245 nucleators that are required for the formation of a cytoplasmic actin mesh that regulates the  
246 magnitude of flows by a yet unknown mechanism. It has been shown in fixed samples that the  
247 removal of the actin mesh seems to cause bundling of MTs in close proximity to the cell cortex.  
248 However, dynamic MT behavior in living mutant oocytes has not been addressed in detail.

249 To monitor the bulk movement of MTs, we imaged cells expressing the MT associated protein  
250 Jupiter::GFP (Jup), which labels the entire MT filament. Compared to control cells, we observed  
251 that MTs in homozygous *capu*<sup>EY12344</sup> or transheterozygous *spire*<sup>1</sup>/*Df(2L)Exel6046* mutant oocytes  
252 appear as thick bundles, which dramatically bend and buckle (Figure 1I-N' and Movie S5). Such  
253 higher 'packing' of filaments does not necessarily indicate their crosslinking, but argues that the  
254 high hydrostatic pressure in fast flowing oocytes is sufficient to bundle MT filaments. More  
255 importantly, and in contrast to previous descriptions, our data demonstrate that in *capu* and *spire*  
256 oocytes MTs cluster even when they are not in close proximity to the cortex, and thus that bundles  
257 can form even when the MTs are not pushed against the cortex. Furthermore, the observed MT  
258 bundles appear longer when compared to control cells, extending further into the posterior (red  
259 arrows in Figure 1L and N). In summary, these results indicate that changing the regime of  
260 cytoplasmic advection impacts on the bulk motion of MTs, as well as on their cytoplasmic  
261 bundling state.

262 In *capu* and *spire* mutant oocytes flows can reach speeds up to 200 nm/s, well within the regime of  
263 plus tip growth. In such mutant situation, the plus tip of single MTs might not be able to 'outgrow'



264 the effect of cytoplasmic advection, and thus flows might become a dominant contributor of MT  
265 orientation. To test whether faster flows alter the orientation of MTs, we quantified the directionality  
266 of EB1 signals in *capu* mutant cells with our OF approach, and found substantial alterations  
267 (Figure 1T-X). Compared to controls, *capu* mutants exhibit large amounts of comets in close  
268 proximity to each other, which move into the same direction. This suggests that *capu* mutant  
269 oocytes display arrays of parallel growing filaments (Figure 1T and Movie S4). The motion of such  
270 EB1 'arrays' (which varies from cell to cell, Figure 1T-X), is likely to correlate with the bundling of  
271 MT filaments described above, and could be interpreted as a direct result of faster flows.  
272 Interestingly, the global posterior EB1 orientation bias was only mildly decreased in most *capu*  
273 mutant oocytes (Figure 1V, W vs. Figure Q, R and Table 1). However, MTs are less focused  
274 towards the posterior tip in *capu* mutants, with only 25% of the posterior-directed EB1 signals  
275 growing with an angle between 30° to 330°. These findings are in a good agreement with the  
276 determinant mis-localization defects in *capu* and *spire* mutant cells (Figure 1X vs. Figure 1K and  
277 M).

278 In summary, these findings together demonstrate that the lack of the actin mesh, and the resulting  
279 increase in flows speeds, impact on the orientation of MTs, and lead us to speculate that at mid-  
280 oogenesis flows must be kept in a precise regime for molecular determinants to be localized  
281 correctly. However, how the actin mesh actually regulates the magnitude of flows in the oocyte is  
282 not known

283

#### 284 **The cytoplasmic actin mesh counteracts the recruitment of Kinesin to MTs *in vivo***

285 The MT plus-tip directed motor protein Kin constitutes the major driving force of cytoplasmic flows  
286 in the *Drosophila* oocyte (Palacios and St Johnston, 2002). To start investigating possible  
287 mechanisms by which the actin mesh regulates the magnitude of cytoplasmic flows, we monitored  
288 the distribution of Kin (Kin1-700-GFP) in control and homozygous *capu*<sup>EY12344</sup> mutant oocytes. This  
289 truncated motor protein lacks all its tail domains, and is thus not autoinhibited and unable to  
290 transport cargo (Williams *et al.*, 2014). In control oocytes, Kin1-700 predominantly localizes to the  
291 posterior of the cell, in a gradient of diminishing abundance from anterior to posterior (Figure 2A  
292 and D, and (Williams *et al.*, 2014)). In stark contrast, Kin1-700 fails to accumulate at the posterior  
293 in *capu* mutant oocytes (Figure 2B and F, Movie S10), and is found instead on filamentous  
294 structures closely resembling MTs (compare Figure 2B to Figure 1L and Movie S10 to Movie S5).  
295 This result indicates that, in the absence of *capu*, Kin becomes strongly recruited to MTs. The  
296 same Kin behavior can be induced acutely by *ex vivo* treatment with F-actin destabilising drugs like  
297 Cytochalasin D (data now shown), indicating that the observed behavior of Kin is due to the lack of  
298 the actin mesh and not to potential developmental defects that might arise from the lack of *capu*  
299 during earlier stages of oogenesis. In fixed control cells, Kin1-700 accumulates to posterior regions  
300 of the cell (Figure 2D), where MTs are less abundant (Figure 2C), while the motor strongly co-

301 localizes with MTs in fixed *capu* mutant oocytes (Figure 2E, F, and J- L). This observation  
302 suggests that the actin mesh alters the ability of Kin to become recruited to MTs.

303 To further understand the relationship between the actin mesh and the interaction of Kin with MTs,  
304 we monitored the localization of the motor in different *capu* mutant alleles. For this, we utilized  
305 three mutant alleles that harbor distinct point mutations in the FH2 domain, and that affect the *in*  
306 *vitro* actin assembly rate of Capu to different degrees (*capu*<sup>L219</sup>, *capu*<sup>L201</sup> and *capu*<sup>38</sup>, in increasing  
307 severity) (Yoo *et al.*, 2015). In order to exclude effects from potential second site mutations, we  
308 generated trans-heterozygous animals between these alleles and the strong hypomorphic mutation  
309 *capu*<sup>EY12344</sup> (Figure 2 and TableS1). In order to estimate the amount of cytoplasmic F-actin, we  
310 measured relative signal intensities in phalloidin-stained control and mutant oocytes (Figure 2M-  
311 Q). In agreement with the *in vitro* data (Yoo *et al.*, 2015), *capu*<sup>L219</sup> oocytes displayed a mild  
312 decrease in signal intensities, followed by *capu*<sup>L201</sup> and *capu*<sup>38</sup>, resulting in the strongest reduction  
313 in fluorescence intensities (Figure 2Q). We next tested the localization of Kin1-700 in these three  
314 allelic combinations of *capu*, and found that in *capu*<sup>L219</sup> oocytes, Kin is found at the posterior region  
315 of the cell (Figure 2R), but also at small MT bundles (arrow in Figure 2R). This recruitment of Kin to  
316 MTs was further enhanced in *capu*<sup>L201</sup> and *capu*<sup>38</sup>, to levels similar to what we observed in the  
317 homozygous *capu*<sup>EY12344</sup> cells (Figure 2S and T, compare to Figure 2B). Thus, the strength of Kin  
318 recruitment to MTs seems to follow the strength of the defects in the actin mesh. It is important to  
319 note that the speed of cytoplasmic flows is equally increased in *capu*<sup>L219</sup>, *capu*<sup>L201</sup> and *capu*<sup>38</sup>  
320 oocytes ((Yoo *et al.*, 2015) and data not shown). Taken together, this indicates that the amount of  
321 Kin recruited to MTs mainly depends on the amount of cytoplasmic F-actin. Together with our  
322 previous finding that a higher number of active Kin results in faster flows (Ganguly *et al.*, 2012),  
323 these findings point towards a model by which the actin mesh is regulating the magnitude of flows  
324 by limiting the efficient recruitment of Kin to MTs.

325

### 326 **Cytoplasmic streaming is necessary for MTs to display a correct orientation**

327 Our results so far show that Kin-dependent cytoplasmic flows need to be maintained at low speeds  
328 in st9 oocytes for MTs not to mis-orient. Consequently, we next asked whether cytoplasmic  
329 streaming might actually be necessary to sustain a proper organization of the MT network. In other  
330 words, is the motion direction of MT plus ends altered in st9 oocytes that lack Kin-dependent  
331 cytoplasmic streaming?

332 To address this question, we first analyzed MTs in oocytes lacking *kinesin heavy chain* (*khc*). The  
333 complete loss of the Kin motor unit (mutant allele *khc*<sup>27</sup>, from hereon called *khc*<sup>null</sup>) results in a fully  
334 penetrant absence of cytoplasmic flows (Figure S8)(Palacios and St Johnston, 2002; Serbus *et al.*,  
335 2005). Compared to control cells, MTs in *khc*<sup>null</sup> mutant oocytes display very little overall motion  
336 and appear rather 'stiff' (Figure 3A,A', compared to Figure 1J,J' and Movie S6). However, oocytes  
337 without Kin do not only lack cytoplasmic streaming, but also lack cargo transport towards the  
338 'posterior tip' and display an aberrant actin mesh (Figure 3D and Figure S9) (Brendza *et al.*, 2000;

339 Drechsler et al., 2017). To test whether the altered bulk behavior of MTs is due to the lack of  
340 streaming or other aberrations in Kin mutant oocytes, we monitored MTs in st9 oocytes carrying  
341 distinct mutations in the Kin motor domain, resulting in a slower motor (two mutant alleles known  
342 as *khc*<sup>23</sup> and *khc*<sup>17</sup>, hereafter summarized as *khc*<sup>slow</sup>) (Brendza et al., 1999). St9 *khc*<sup>slow</sup> oocytes  
343 display a normal cytoplasmic actin mesh (Figure S9) and are able to transport a considerable  
344 amount of cargo towards the posterior (Figure 3E and F) (Serbus et al., 2005; Loiseau et al.,  
345 2010). Importantly, and identical to *khc*<sup>null</sup> cells, they lack any cytoplasmic advection at st9,  
346 allowing us to study the impact of flows on MT behavior in the presence of transport (Figure  
347 S8)(Serbus et al., 2005). Similar to *khc*<sup>null</sup> cells, MTs in *khc*<sup>slow</sup> oocytes appear stiff and no motion  
348 could be detected in kymographs (Figure 3B-C' and Movie S6). These observations indicate that  
349 the altered motion of MTs in oocytes without Kin is indeed due to a lack of cytoplasmic streaming.  
350 Thus, Kin-dependent cytoplasmic advection is necessary for MTs to display a wild-type bulk  
351 motion.

352 We next analyzed EB1 directionality in *khc*<sup>slow</sup> oocytes (Figure 3G-K). As in control cells, we  
353 observed dynamic EB1 comets throughout the entire cytoplasm (Movie S7). However, in stark  
354 contrast, the distribution of orientation angles displayed a more focused bias towards the posterior  
355 of the cell (Figure 3I vs. Figure 1Q). Consequently, *khc*<sup>slow</sup> mutant oocytes displayed an increased  
356 posterior plus-tip bias, with 75% of EB1 signals directed towards posterior, compared to 66% in  
357 control cells (Figure 3J vs. Figure 1R and Table 1). Furthermore, 54% of these posterior-directed  
358 EB1 signals (the group consisting of 75% of all comets) displayed a 'posterior tip' orientation,  
359 compared to 40% in controls (Figure 3K vs. Figure 1S and Table 1). These findings indicate that  
360 the orientation of the growing MT plus ends in st9 oocytes does not only depend on nucleation or  
361 anchoring of minus ends, but also on the presence of cytoplasmic flows. In other words, advection  
362 is necessary for MTs to display a correct orientation.

363 To further investigate the impact of cytoplasmic flows and Kin activity on MT orientation, we  
364 analyzed the regional organization of the MT network along the A-P axis in control, *khc*<sup>null</sup> and  
365 *khc*<sup>slow</sup> oocytes. We divided each oocyte into an anterior and a posterior region (Figure 4A), and  
366 analyzed EB1 directionality in each of these two regions (Table 1). As previously shown, the  
367 posterior EB1 bias increases along the A-P axis of st9 oocytes (Figure 4B-D) (Parton et al., 2011).  
368 In the anterior region, we found 62% of signals directed towards posterior (Figure 4C), while this  
369 bias was increased to 74% in the posterior region (Figure 4D). As already demonstrated for the  
370 global posterior EB1 bias (Figure 4B), *khc*<sup>slow</sup> oocytes also showed a dramatic change of MT  
371 orientation along the A-P axis, with a 74% posterior bias in the anterior region (Figure 4E vs.  
372 Figure 4C) and an even further increased 81% posterior bias in the posterior region (Figure 4F vs.  
373 Figure 4D). Additionally, the ratio of signals directed towards the 'posterior tip' (Figure 1C) in both  
374 anterior and posterior regions of the *khc*<sup>slow</sup> cell was substantially increased, compared to controls  
375 (Figure 4E and F, and Table 1). This clearly demonstrates that oocytes with a slower Kin, and thus  
376 without cytoplasmic streaming, display a stronger polarization of the entire MT network towards the

377 posterior pole, a key region in the establishment of the embryonic body axis. While the lack of Kin  
378 (*khc<sup>null</sup>*) seemed to cause only minor defects in the global organization of the MT cytoskeleton  
379 (Figure 3L-Pand Figure 4B), the regional analysis of EB1 directionality in *khc<sup>null</sup>* oocytes revealed  
380 major differences compared to control cells. In the anterior region of *khc<sup>null</sup>* cells, we detected an  
381 unexpected drop of the posterior bias (56% compared to 66% in controls), which indicates that the  
382 complete lack of Kin does indeed affect MT network organization (Figure 4G vs. Figure 4C). It  
383 needs to be mentioned here that oocytes lacking Kin also fail to localize the nucleus, which in turn  
384 is associated with MT minus ends (Williams et al., 2014). Therefore, this observed MT behavior in  
385 *khc<sup>null</sup>* cells might primarily reflect the mis-localization of a certain subset of MTOCs in the cell.  
386 However, MTs in the posterior region of *khc<sup>null</sup>* cells displayed a slightly more focused growth  
387 towards the key 'posterior tip' (Figure 1C), similar to *khc<sup>slow</sup>* cells (Figure 4H vs. Figure 4D and F,  
388 right rosette panels, and Table 1).

389 Taken together, our data allow us to draw certain conclusions about the relationship of Kin-activity,  
390 cytoplasmic streaming, and the organization of MTs. Firstly, in st9 oocytes cytoplasmic flows need  
391 to be in a defined regime to ensure proper MT orientation. Secondly, in the presence of Kin-  
392 mediated transport, but in the absence of cytoplasmic flows (*khc<sup>slow</sup>* condition), there are more plus  
393 ends growing towards the posterior, suggesting that cytoplasmic streaming is necessary for MTs to  
394 polarize in the precise pattern observed in control cells. And thirdly, together with cytoplasmic  
395 flows, other Kin-mediated processes, such as cargo transport or nucleus anchoring affect the  
396 organization of the MT network, supporting previously published findings (Nieuwburg et al., 2017;  
397 Zimyanin et al., 2008).

398

### 399 **Reconstitution of cytoplasmic flows in st9 *khc<sup>slow</sup>* oocytes rescues MT orientation**

400 Our data suggest that Kin-mediated cytoplasmic streaming is necessary for the MT network to  
401 completely adopt its wild-type organization in the st9 oocyte. To further investigate the connection  
402 between cytoplasmic advection and MT orientation, we analyzed EB1 directionality in *capu, khc<sup>slow</sup>*  
403 double mutant oocytes. With this experiment we aimed to test whether the re-establishment of  
404 cytoplasmic streaming in a mutant background is sufficient to rescue MT orientation.

405 It has been suspected that faster cytoplasmic flows in *capu* mutants can be slowed down again by  
406 introducing a *khc<sup>slow</sup>* mutation (Dahlgaard et al., 2007). Therefore, we generated a double mutant,  
407 harboring the alleles *capu<sup>EY12344</sup>* and *khc<sup>17</sup>*. To verify the functionality of this double mutant, we first  
408 investigated posterior cargo localization in fixed cells. As expected, ~85% of *capu, khc<sup>slow</sup>/+* cells  
409 (which are essentially *capu* mutants, Table S1) failed to correctly localize Staufen to the posterior  
410 pole of the cell (Figure 5A, n=20). In comparison, ~72% of *capu, khc<sup>slow</sup>* double mutant cells  
411 localized Staufen into a posterior crescent (n=25). However, the majority of oocytes that displayed  
412 Staufen in a crescent, also showed Staufen accumulation in posterior dots (n=11/18). This  
413 constitutes a phenotype that is usually associated with the *khc<sup>slow</sup>* alleles (Figure 5B vs. Figure 3E  
414 and F). Together, these data confirmed that our double mutant is comparable to the previously

415 reported alleles (Dahlgard et al., 2007), and that slow Kin is sufficient to rescue the major cargo  
416 localization defects seen in *capu* mutants. However, since cargo transport was not rescued to wild-  
417 type levels, and was instead found to be similar to *khc<sup>slow</sup>* oocytes (Loiseau et al., 2010), it is  
418 obvious that the decreased cargo transport efficiency of slow Kin cannot be rescued by re-  
419 introducing cytoplasmic streaming by the lack of *capu*. It is furthermore unclear whether this is due  
420 to a reduced translocation speed of slow Kin, or to a defect in cargo anchoring in *capu* mutant cells  
421 (Tanaka et al., 2011).

422 Next we tested whether premature fast cytoplasmic flows in *capu* mutants are indeed slowed down  
423 again in *capu,khc<sup>slow</sup>* oocytes. As expected, and similar to *capu* single mutants, *capu,khc<sup>slow</sup>/+*  
424 oocytes displayed aberrant fast flows (Figure 5C, Movie S8). In contrast, cytoplasmic flows in  
425 *capu,khc<sup>slow</sup>* double mutant oocytes were indeed slowed down again and appeared similar to those  
426 observed in control cells (Figure S8). We then tested whether the rescue of cytoplasmic streaming  
427 in the double mutant also affected MT bulk movement. Compared to *capu,khc<sup>slow</sup>/+* oocytes, which  
428 displayed fast flows and consequently MT bundeling, the reduction of flow speeds in the double  
429 mutant caused a MT bulk movement similar to that observed in control cells (Figure 5C-D' and  
430 Movie S8).

431 To finally test whether the re-establishment of cytoplasmic streaming in a *khc<sup>slow</sup>* background (or  
432 the reduction of fast flows in *capu* background) rescues the MT orientation defects observed in  
433 either single mutant, we analyzed EB1 directionality in *capu,khc<sup>slow</sup>/+* (Figure 5E-I) and *capu,khc<sup>slow</sup>*  
434 double mutant oocytes (Figure 5J-N and Movie S9). EB1 comets in *capu,khc<sup>slow</sup>/+* oocytes  
435 exhibited values that are similar to what we observed in *capu* mutants (Figure 1T-X), suggesting  
436 that the heterozygous presence of a *khc<sup>slow</sup>* mutant chromosome does not substantially affect the  
437 *capu* mutant phenotype (Movie S9, 61% of EB1 signals pointing towards posterior, and 34% of this  
438 61% are growing towards the 'posterior tip' in *capu,khc<sup>slow</sup>/+* cells, Figure 5F-I and Table 1).  
439 Conversely, EB1 comets in *capu,khc<sup>slow</sup>* double mutant cells displayed a posterior motion bias  
440 indistinguishable from that of control cells (Movie S9, 66% posterior bias, Figure 5M vs. Figure 1R  
441 and Table 1). Finally, also the fraction of all posterior comets pointing towards the 'posterior tip'  
442 was found to be similar in *capu,khc<sup>slow</sup>* double mutant cells (39%) and controls (40%) (Figure 5N  
443 vs. Figure 1S and Table 1), further strengthening the idea that cytoplasmic streaming constitutes a  
444 substantial contributor to a correct MT plus end focussing, and thus MT organization, in the oocyte.

445 In summary, our results now clearly demonstrate that in the absence of *capu* and the actin mesh, a  
446 slower Kin motor protein is sufficient to restore the correct regime of cytoplasmic flows, resulting in  
447 the correct polarization of the MT cytoskeleton, and an almost restored transport of cargo towards  
448 the posterior. Therefore, it seems that the actin mesh is essential in oocytes that exhibit normal  
449 Kin-mediated transport, likely by regulating the amount of Kin recruited to MTs, in order to ensure  
450 the proper regulation of cytoplasmic streaming, which in turn is an important contributor to the  
451 observed MT orientation.

## 452 DISCUSSION

453 Due to its large size (80-100  $\mu\text{m}$  along the A-P axis) and the fact that MT minus ends are  
454 nucleated and anchored along the antero-lateral cortices of the cell, the *Drosophila* st9 oocyte is  
455 arguably one of the most challenging *in vivo* systems in which to analyze the dynamic behavior of  
456 MTs. The use of confocal microscopy, together with OF based analysis tool described in this study,  
457 allowed us to quantify the motion direction of plus ends within a 2D focal plane along the entire  
458 length of this cell. Together with others, the present study supports the existence of a complex  
459 mechanical and/or biochemical relationship between motion of cytoplasmic components (whether  
460 by advection or by transport), cytoplasmic F-actin and MTs in the *Drosophila* oocyte. This holds  
461 true for our model system, but is likely transferable to many other cell types. For example,  
462 experimental data and modeling of cytoplasmic motion in Characean algae (where cytoplasmic  
463 flows are acto-myosin dependent) suggests that parallel actin cables and ordered streaming  
464 patterns self-organize in an interdependent manner (Foissner and Wasteneys, 2000; Woodhouse  
465 and Goldstein, 2013).

466 Kin-mediated cargo transport through a highly viscous medium, such as the cytoplasm, inevitably  
467 induces bulk motion of such medium, which will cause lateral displacement forces on MT filaments  
468 and thus induce a feedback on their spatial orientation. As a consequence, cytoplasmic streaming  
469 needs to be kept in a defined speed regime and at a biased random pattern in order for the MT  
470 network to properly polarize. In the absence of the actin mesh (as in *capu* or *spire* mutants), there  
471 is an increased persistence and speed of flows, resulting in parallel alignment and bundling of  
472 MTs, as well as strong defects on MT orientation. The actin mesh - which itself requires Kin activity  
473 for its proper organization (Drechsler et al., 2017) - is required for the maintenance of this correct  
474 regime of advection.

475 With our work, we show that our image analysis approach - based on a rigorous image analysis  
476 framework - is able to infer and quantify directionality of EB1 motion from confocal image  
477 sequences. The use of an efficient iterative optimisation algorithm enabled us to analyze entire  
478 image sequences at once, as compared to a frame-by-frame analysis. In comparison to more  
479 commonly used techniques, such as particle tracking or PIV, OF allows us to perform motion  
480 estimation on pixel level in challenging circumstances, such as low signal-to-noise ratios and small  
481 particle size. Most importantly, this image analysis approach can handle standard confocal  
482 microscopy data and the method does not require demanding imaging techniques or costly  
483 computing hardware. Moreover, the image analysis depends only on a few parameters that can be  
484 easily adjusted. However, two limitations of the developed methodology need to be pointed out.  
485 Firstly, due to the use of a variational framework for the image analysis, both the denoised  
486 sequences and the estimated velocities exhibit a loss of contrast, leading to underestimated  
487 speeds of EB1 comets. This is particularly due to the temporal regularization required in both steps  
488 to overcome the above-mentioned challenges. Secondly, our statistical analyses of directions of  
489 EB1 comets are based on velocities computed for all pixels within each segmented oocyte. We are

490 aware that not every image pixel portrays exactly one EB1 comet. Furthermore, EB1 comets in the  
491 oocyte are subjected to different forces. In summary however, our results demonstrate that our  
492 approach is able to monitor general plus end direction in most, if not all, cell types and thus  
493 constitutes an efficient and reliable analytical framework for MT polarity studies. Therefore, OF is  
494 absolutely suitable to efficiently describe the orientation of MTs in crowded intracellular  
495 environments.

496 It is unknown how the actin mesh slows down Kin-dependent cytoplasmic flows or how it might  
497 affect MT organization. It has been proposed that the presence of a viscoelastic actin network can  
498 increase the effective viscosity of the cytoplasm, and counteract the viscous drag of cargo  
499 transport by Kin (Quinlan, 2016). Furthermore, actin-MT crosslinking proteins have been  
500 demonstrated to allow a potent crosstalk between both filament species (Preciado Lopez *et al.*,  
501 2014), presumably coordinating cytoskeletal organization *in vivo*. However, our data from  
502 *capu,khc<sup>slow</sup>* double mutant oocytes, which do not form an actin mesh, suggest that the mesh itself  
503 is not essential to allow a correct MT orientation when Kin is slower. In this 'artificial' mutant  
504 situation, the correct regime of flows seems sufficient to allow proper MT network organization. It is  
505 thus possible that the actin mesh regulates the activity of Kin more directly, for example by  
506 tethering the motor to its filaments (directly or indirectly through cargo). Such model is indeed  
507 supported by our finding that Kin becomes efficiently recruited to MTs when the actin mesh is  
508 absent (Movie S10 and Figure 2). This observation could explain how the mesh regulates not only  
509 flows, but also the higher degree of MT bundling, as a larger number of Kin molecules recruited to  
510 MTs is likely to result in faster flows (Ganguly *et al.*, 2012). Furthermore, this could also result in a  
511 higher degree of effective crosslinking of adjacent filaments (Lu *et al.*, 2016). However, the  
512 recruitment of Kin to MTs depends on various regulatory mechanisms, including interactions with  
513 cargo and MT-associated proteins like Ensconsin (Metivier *et al.*, 2019). For this reason we used  
514 the truncated form Khc1-700 in our analyses. Whether, and how, the actin mesh influences the  
515 interaction of full length Kin with MTs - in the presence of other MT-binding regulatory mechanisms  
516 - needs to be further addressed in the future. Nevertheless, our findings indicate a novel potential  
517 mechanism of how the actin and MT cytoskeletons can regulate each other.

518 Our data establish cytoplasmic streaming in st9 oocytes as a contributing factor for the correct  
519 organization of the MT cytoskeleton. If - and how - a stronger posterior polarization of the MT  
520 network may affect cargo delivery to the posterior is unknown. Tracking *oskar* mRNA particles in  
521 *khc<sup>slow</sup>* oocytes did not reveal a stronger orientation bias of cargo movement (Zimyanin *et al.*,  
522 2008). However, it is unclear whether trajectories of *oskar* transport always reflect the organization  
523 of the underlying MT network, and whether all MTs would be equally used by slow Kin motor/cargo  
524 complexes.

525 Previous studies suggested that the pattern of nucleation and minus end anchoring along the  
526 cortex are sufficient to organize the MT network and to allow correct cargo transport to define the

527 A-P axis of the animal. Consequently, mutant oocytes harboring defects in nucleation and/or  
528 anchoring of minus ends also display polarity defects (Doerflinger et al., 2006; Nashchekin et al.,  
529 2016). Furthermore, mathematical modeling suggested that cytoplasmic streaming at mid-  
530 oogenesis is negligible to explain the correct localization of posterior cargoes like *oskar* mRNA  
531 (Khuc Trong et al., 2015). However, our study demonstrates that cytoplasmic streaming is involved  
532 in the orientation of MT plus ends, and we conclude that the localization of the minus ends alone is  
533 not sufficient to define the precise overall organization of the network. This was most obvious in  
534 *khc<sup>slow</sup>* oocytes, which in our hands lack cytoplasmic streaming entirely, and displayed an  
535 increased posterior orientation MT bias (Figure 3). The advantage of analyzing slow Kin mutants is  
536 that other Kin-dependent processes, like cargo transport and formation of the actin mesh, do take  
537 place. Despite showing only mild defects in the distribution of developmental determinants, *khc<sup>slow</sup>*  
538 mutant oocytes fail to give rise to a healthy offspring, suggesting that oocyte polarity is affected  
539 (Moua et al., 2011). Consistently, we found an increased posterior bias of EB1 signals in *khc<sup>slow</sup>*  
540 mutant oocytes, strongly suggesting that the lack of cytoplasmic streaming was causative for this  
541 observation.

542 In summary, the combination of various forces produced within living cells demands a complex set  
543 of biochemical and biomechanical regulatory mechanisms for cytoskeletal networks to organize  
544 correctly. Our results show that, in *Drosophila* st9 oocytes, advection by cytoplasmic streaming  
545 contributes to the polarization of MTs by affecting the directional motion of MT plus ends. All these  
546 observations further stress the need for a combination of different experimental approaches in  
547 order to fully understand the dynamic organization of cytoskeletons, from simplified *in vitro*  
548 systems to complex *in vivo* situations.



## 549 **METHODS**

### 550 **Fly stocks and genetics**

551 Flies were kept at standard corn meal agar and raised at room temperature (21°C). Detailed  
552 genotypes of all fly stocks can be found in Table S1. Germ line clones for the analysis of *khc*  
553 mutant alleles have been induced by the FLP/FRT ovoD system (Chou and Perrimon, 1996).  
554 Germline clones in Figure 5 were identified by the absence of nuclear GFP in germline cells.

555

### 556 **Live imaging**

557 Female flies of the desired genotypes were collected and fattened on dry yeast for 12-16 h prior to  
558 imaging. Ovaries were dissected in a small drop of halocarbon oil (Votalef S10, VWR) on a glass  
559 coverslip and single egg chambers were separated using fine tungsten needles. Images were  
560 acquired on a Leica SP5 inverted confocal microscope, using a 40x/1.3 Oil DIC Plan-Neofluar  
561 (Jup) or a 100x/1.4 Oil DIC objective (EB1). Signals were detected using a Leica HyD Hybrid  
562 Detector. For MT bulk movement, a single plane from the middle of the oocyte was imaged at a  
563 scan speed of 100 Hz and at an image resolution of 1,024 × 1,024 pixels (corresponding to one  
564 image every 10.4 s). For EB1 imaging the oocyte was fitted and oriented within a 512 x 256 pixels  
565 frame and a single plane image was taken every 0.65 s. Image sequences of at least 100 frames  
566 (65 s) were taken, inspected visually, and bleach corrected using Fiji (Schindelin *et al.*, 2012). In all  
567 experiments the middle of the oocyte was defined as the focal plane in which the oocyte had its  
568 largest area.

569

### 570 **Immunostainings**

571 Egg chambers were dissected in PBS+0.1% Tween20 and fixed in 10% formaldehyde in  
572 PBS+0.1% Tween20 for 10 min. Fixed ovaries were incubated with anti- $\alpha$ Tubulin (MAB1864,  
573 Sigma-Aldrich, cloneYL1/2, 1:100) or anti-Staufen (gift from. D. St Johnston, 1:3,000) in PBS+2%  
574 Tween20 over night at 4°C. After four consecutive washes Alexa-coupled secondary antibodies  
575 (1:100) were incubated for two hours at room temperature. Native fluorescence of GFP was  
576 imaged without amplification. Images were acquired on a Leica SP5 inverted confocal microscope,  
577 using a 40x/1.3 Oil DIC Plan-Neofluar objective. For phalloidin staining, egg chambers were  
578 dissected and fixed in 10% methanol free formaldehyde in PBS, containing 0.1% Tween-20  
579 (PBT0.1), for a maximum of 10 min. Fixed cells were washed 4x in PBT0.1 and incubated with  
580 1  $\mu$ M TRITC-coupled phalloidin (in PBT0.1, Sigma-Aldrich) over night at 4°C. The stained  
581 samples were washed 4x in PBT0.1, mounted, and imaged immediately under identical conditions,  
582 using a Zeiss LSM800 equipped with a 40x/1.3 Oil DIC Plan-Neofluar objective. Normalized  
583 fluorescence intensities were acquired using Fiji.

584

585

586

## 587 **Image denoising and optical flow based motion estimation**

588 Motion analysis of the recorded two-dimensional image sequences was performed using a two-  
589 step procedure. The first step aimed to remove noise contamination from the unprocessed  
590 sequences, while the goal of the second step was to estimate motion in terms of displacement  
591 vector fields from the so-improved sequences. As noise may significantly disturb the motion  
592 estimation (Ruhnau et al., 2005; Burger *et al.*, 2018), this two-step procedure is crucial for  
593 obtaining robust estimation results. In the first step, we recovered from each recorded image  
594 sequence  $u^\delta$  an improved version  $u$  by solving a variational image denoising problem with spatio-  
595 temporal regularization. It reads

$$u = \operatorname{argmin}_u \frac{1}{2} \|u - u^\delta\|^2 + \alpha_1 \|\nabla u\|_{2,1} + \frac{\beta_1}{2} \|\partial_t u\|^2.$$

596 While the first two terms on the right-hand side resemble standard image denoising with total  
597 variation regularization (Rudin L.I, 1992) in space, the third term connects subsequent frames by  
598 penalising temporal changes within the recovered solution. As EB1 comets typically appear in  
599 several subsequent frames at similar positions, it allows to effectively remove randomly distributed  
600 noise from a sequence (see Figure 2D,E, Movie S2, and SI). Here,  $\alpha, \beta > 0$  are regularization  
601 parameters that balance the three terms and need to be chosen appropriately. Moreover, the  
602 norms (as defined in equation S21) are taken over the entire image sequence.

603 The result  $u$  served as input to the motion estimation step, in which we estimated a displacement  
604 vector field  $\vec{v} = (v_1, v_2)^T$  by solving

$$\vec{v} = \operatorname{argmin}_{\vec{v}} \frac{1}{2} \|\partial_t u + \langle \nabla u, \vec{v} \rangle\|^2 + \alpha_2 \|\nabla \vec{v}\|_{2,1} + \frac{\beta_2}{2} \|\partial_t \vec{v}\|_{2,2}^2.$$

605 Here,  $\vec{v} = \vec{v}(x)$  is defined for every pixel  $x$  of the image  $u$  and is an estimate of the motion that  $u$   
606 experiences at  $x$  from one image frame to the subsequent one in time. That is, the vector  $\vec{v}(x) =$   
607  $(v_1(x), v_2(x))^T$  points in the direction of motion at  $x$ , and  $|\vec{v}(x)|$  is an estimate of the speed of the  
608 motion at  $x$ . The first term on the right-hand side in the above equation aims to approximately  
609 solve the optical flow equation (Horn and Schunck, 1981), while the second and third terms  
610 incorporate spatio-temporal regularization of the vector-valued unknown (for further details see SI).  
611 The use of the vector-valued total variation allows for spatial discontinuities in the displacement  
612 vector field. We found that in both steps the temporal regularization was key and the analysis of  
613 individual frames did not yield satisfactory results. Both minimisation problems were approximately  
614 solved using the primal-dual hybrid gradient method (Chambolle, 2011) and graphics-processing  
615 unit (GPU) acceleration. An in-depth description of both models, their numerical solution, and  
616 parameter choices as well as implementation details can be found in the SI.

617

618 **REFERENCES**

- 619
- 620 Akhmanova, A., and Steinmetz, M.O. (2015). Control of microtubule organization and dynamics:  
621 two ends in the limelight. *Nat Rev Mol Cell Biol* *16*, 711-726.
- 622
- 623 Amat, F., Myers, E.W., and Keller, P.J. (2013). Fast and robust optical flow for time-lapse  
624 microscopy using super-voxels. *Bioinformatics* *29*, 373-380.
- 625
- 626 Baker, S., Scharstein D, Lewis J.P, Roth S, Black M.J, and Szeliski R. (2011). A database and  
627 evaluation methodology for optical flow. *Int. J. Comput. Vision* *92(1)*, 1–31.
- 628
- 629 Boquet-Pujadas, A., Lecomte, T., Manich, M., Thibeaux, R., Labruyere, E., Guillen, N., Olivo-Marin,  
630 J.C., and Dufour, A.C. (2017). BioFlow: a non-invasive, image-based method to measure speed,  
631 pressure and forces inside living cells. *Sci Rep* *7*, 9178.
- 632
- 633 Boric, K., Orio, P., Vieville, T., and Whitlock, K. (2013). Quantitative analysis of cell migration using  
634 optical flow. *PLoS One* *8*, e69574.
- 635
- 636 Brendza, R.P., Serbus, L.R., Duffy, J.B., and Saxton, W.M. (2000). A function for Kinesin I in the  
637 posterior transport of *oskar* mRNA and Stauf protein. *Science* *289*, 2120-2122.
- 638
- 639 Burger, M., Dirks, H., and Schönlieb, C.-B. (2018). A Variational Model for Joint Motion Estimation  
640 and Image Reconstruction. *Siam Journal on Imaging Sciences* *11*, 94-128.
- 641
- 642 Chambolle, A.P., T. . (2011). A first-order primal-dual algorithm for convex problems with  
643 applications to imaging. . *J. Math. Imaging Vis.* *40*, 120–145.
- 644
- 645 Chou, T.B., and Perrimon, N. (1996). The autosomal FLP-DFS technique for generating germline  
646 mosaics in *Drosophila melanogaster*. *Genetics* *144*, 1673-1679.
- 647
- 648 Dahlgaard, K., Raposo, A.A., Niccoli, T., and St Johnston, D. (2007). Capu and Spire assemble a  
649 cytoplasmic actin mesh that maintains microtubule organization in the *Drosophila* Oocyte. *Dev Cell*  
650 *13*, 539-553.
- 651
- 652 Delpiano, J., Jara J, Scheer J, Ramirez O.A, Ruiz-del-Solar J, and S., H. (2012). Performance of  
653 optical flow techniques for motion analysis of fluorescent point signals in confocal microscopy.  
654 *Machine Vision and Applications* *23*, 675–689.
- 655
- 656 Doerflinger, H., Benton, R., Torres, I.L., Zwart, M.F., and St Johnston, D. (2006). *Drosophila*  
657 anterior-posterior polarity requires actin-dependent PAR-1 recruitment to the oocyte posterior.  
658 *Curr Biol* *16*, 1090-1095.
- 659
- 660 Drechsler, M., Giavazzi, F., Cerbino, R., and Palacios, I.M. (2017). Active diffusion and advection in  
661 *Drosophila* oocytes result from the interplay of actin and microtubules. *Nat Commun* *8*, 1520.
- 662
- 663 Fassier, C., Freal, A., Gasmi, L., Delphin, C., Ten Martin, D., De Gois, S., Tambalo, M., Bosc, C.,  
664 Mailly, P., Revenu, C., Peris, L., Bolte, S., Schneider-Maunoury, S., Houart, C., Nothias, F., Larcher,  
665 J.C., Andrieux, A., and Hazan, J. (2018). Motor axon navigation relies on Fidgetin-like 1-driven  
666 microtubule plus end dynamics. *J Cell Biol* *217*, 1719-1738.

- 667 Foissner, I., and Wasteneys, G.O. (2000). Microtubule disassembly enhances reversible  
668 cytochalasin-dependent disruption of actin bundles in characean internodes. *Protoplasma* *214*, 33-  
669 44.  
670
- 671 Forrest, K.M., and Gavis, E.R. (2003). Live imaging of endogenous RNA reveals a diffusion and  
672 entrapment mechanism for nanos mRNA localization in *Drosophila*. *Curr Biol* *13*, 1159-1168.  
673
- 674 Frerking, L., Burger, M., Vestweber, D., and C., B. (2014). TGV-based flow estimation for 4D  
675 leukocyte transmigration. A. K. Louis, S. Arridge, and B. Rundell, editors, Proceedings of the  
676 Inverse Problems from Theory to Applications Conference, 79–83.  
677
- 678 Ganguly, S., Williams, L.S., Palacios, I.M., and Goldstein, R.E. (2012). Cytoplasmic streaming in  
679 *Drosophila* oocytes varies with kinesin activity and correlates with the microtubule cytoskeleton  
680 architecture. *Proc Natl Acad Sci U S A* *109*, 15109-15114.  
681
- 682 Gonzalez-Reyes, A., Elliott, H., and St Johnston, D. (1995). Polarization of both major body axes in  
683 *Drosophila* by gurken-torpedo signalling. *Nature* *375*, 654-658.  
684
- 685 Guo, v.d.V., and Zhou. (2014). Red blood cell tracking using optical flow methods. *IEEE J. Biomed.*  
686 *Health Inform* *18(3)*, 991-998.  
687
- 688 Huang, Y., Hao, L., Li, H., Liu, Z., and Wang, P. (2017). Quantitative Analysis of Intracellular Motility  
689 Based on Optical Flow Model. *J Healthc Eng* *2017*.  
690
- 691 Hurd, T.R., Herrmann, B., Sauerwald, J., Sanny, J., Grosch, M., and Lehmann, R. (2016). Long Oskar  
692 Controls Mitochondrial Inheritance in *Drosophila melanogaster*. *Dev Cell* *39*, 560-571.  
693
- 694 Januschke, J., Gervais, L., Dass, S., Kaltschmidt, J.A., Lopez-Schier, H., Johnston, D.S., Brand, A.H.,  
695 Roth, S., and Guichet, A. (2002). Polar transport in the *Drosophila* oocyte requires Dynein and  
696 Kinesin I cooperation. *Curr Biol* *12*, 1971-1981.  
697
- 698 Jiang, K., Toedt, G., Montenegro Gouveia, S., Davey, N.E., Hua, S., van der Vaart, B., Grigoriev, I.,  
699 Larsen, J., Pedersen, L.B., Bezstarosti, K., Lince-Faria, M., Demmers, J., Steinmetz, M.O., Gibson,  
700 T.J., and Akhmanova, A. (2012). A Proteome-wide screen for mammalian SxIP motif-containing  
701 microtubule plus-end tracking proteins. *Curr Biol* *22*, 1800-1807.  
702
- 703 Kent, I.A., Rane, P.S., Dickinson, R.B., Ladd, A.J., and Lele, T.P. (2016). Transient Pinning and  
704 Pulling: A Mechanism for Bending Microtubules. *PLoS One* *11*, e0151322.  
705
- 706 Khuc Trong, P., Doerflinger, H., Dunkel, J., St Johnston, D., and Goldstein, R.E. (2015). Cortical  
707 microtubule nucleation can organise the cytoskeleton of *Drosophila* oocytes to define the  
708 anteroposterior axis. *Elife* *4*.  
709
- 710 Kodama, A., Karakesisoglou, I., Wong, E., Vaezi, A., and Fuchs, E. (2003). ACF7. An essential  
711 integrator of microtubule dynamics. *Cell* *115*, 343-354.  
712
- 713 Loiseau, P., Davies, T., Williams, L.S., Mishima, M., and Palacios, I.M. (2010). *Drosophila* PAT1 is  
714 required for Kinesin-1 to transport cargo and to maximize its motility. *Development* *137*, 2763-  
715 2772.

- 716 Lu, W., Lakonishok, M., Serpinskaya, A.S., Kirchenbuechler, D., Ling, S.C., and Gelfand, V.I. (2018).  
717 Ooplasmic flow cooperates with transport and anchorage in *Drosophila* oocyte posterior  
718 determination. *J Cell Biol* *217*, 3497-3511.  
719
- 720 Lu, W., Winding, M., Lakonishok, M., Wildonger, J., and Gelfand, V.I. (2016). Microtubule-  
721 microtubule sliding by kinesin-1 is essential for normal cytoplasmic streaming in *Drosophila*  
722 oocytes. *Proc Natl Acad Sci U S A* *113*, E4995-5004.  
723
- 724 Metivier, M., Monroy, B.Y., Gallaud, E., Caous, R., Pascal, A., Richard-Parpaillon, L., Guichet, A., Ori-  
725 McKenney, K.M., and Giet, R. (2019). Dual control of Kinesin-1 recruitment to microtubules by  
726 Ensconsin in *Drosophila* neuroblasts and oocytes. *Development* *146*.  
727
- 728 Mitchison, T., and Kirschner, M. (1984). Dynamic instability of microtubule growth. *Nature* *312*,  
729 237-242.  
730
- 731 Monteith, C.E., Brunner, M.E., Djagaeva, I., Bielecki, A.M., Deutsch, J.M., and Saxton, W.M. (2016).  
732 A Mechanism for Cytoplasmic Streaming: Kinesin-Driven Alignment of Microtubules and Fast Fluid  
733 Flows. *Biophys J* *110*, 2053-2065.  
734
- 735 Moua, P., Fullerton, D., Serbus, L.R., Warrior, R., and Saxton, W.M. (2011). Kinesin-1 tail  
736 autoregulation and microtubule-binding regions function in saltatory transport but not ooplasmic  
737 streaming. *Development*.  
738
- 739 Nashchekin, D., Fernandes, A.R., and St Johnston, D. (2016). Patronin/Shot Cortical Foci Assemble  
740 the Noncentrosomal Microtubule Array that Specifies the *Drosophila* Anterior-Posterior Axis. *Dev*  
741 *Cell* *38*, 61-72.  
742
- 743 Nieuwburg, R., Nashchekin, D., Jakobs, M., Carter, A.P., Khuc Trong, P., Goldstein, R.E., and St  
744 Johnston, D. (2017). Localised dynactin protects growing microtubules to deliver oskar mRNA to  
745 the posterior cortex of the *Drosophila* oocyte. *Elife* *6*.  
746
- 747 Palacios, I.M., and St Johnston, D. (2002). Kinesin light chain-independent function of the Kinesin  
748 heavy chain in cytoplasmic streaming and posterior localisation in the *Drosophila* oocyte.  
749 *Development* *129*, 5473-5485.  
750
- 751 Parton, R.M., Hamilton, R.S., Ball, G., Yang, L., Cullen, C.F., Lu, W., Ohkura, H., and Davis, I. (2011).  
752 A PAR-1-dependent orientation gradient of dynamic microtubules directs posterior cargo  
753 transport in the *Drosophila* oocyte. *J Cell Biol* *194*, 121-135.  
754
- 755 Preciado Lopez, M., Huber, F., Grigoriev, I., Steinmetz, M.O., Akhmanova, A., Koenderink, G.H., and  
756 Dogterom, M. (2014). Actin-microtubule coordination at growing microtubule ends. *Nat Commun*  
757 *5*, 4778.  
758
- 759 Purro, S.A., Ciani, L., Hoyos-Flight, M., Stamatakou, E., Siomou, E., and Salinas, P.C. (2008). Wnt  
760 regulates axon behavior through changes in microtubule growth directionality: a new role for  
761 adenomatous polyposis coli. *J Neurosci* *28*, 8644-8654.  
762
- 763 Quinlan, M.E. (2013). Direct interaction between two actin nucleators is required in *Drosophila*  
764 oogenesis. *Development* *140*, 4417-4425.

765 Quinlan, M.E. (2016). Cytoplasmic Streaming in the *Drosophila* Oocyte. *Annu Rev Cell Dev Biol* 32,  
766 173-195.  
767  
768 Roth, S., Neuman-Silberberg, F.S., Barcelo, G., and Schupbach, T. (1995). *cornichon* and the EGF  
769 receptor signaling process are necessary for both anterior-posterior and dorsal-ventral pattern  
770 formation in *Drosophila*. *Cell* 81, 967-978.  
771  
772 Rudin L.I, O.S., and Fatemi E. (1992). Nonlinear total variation based noise removal algorithms.  
773 *Physica D: Nonlinear Phenomena* 60, 259-268.  
774  
775 Ruhnau et al. (2005). Variational optical flow estimation for particle image velocimetry. *Expe.*  
776 *Fluids* 38(1), 21–32.  
777  
778 Schindelin, J., Arganda-Carreras, I., Frise, E., Kaynig, V., Longair, M., Pietzsch, T., Preibisch, S.,  
779 Rueden, C., Saalfeld, S., Schmid, B., Tinevez, J.Y., White, D.J., Hartenstein, V., Eliceiri, K., Tomancak,  
780 P., and Cardona, A. (2012). Fiji: an open-source platform for biological-image analysis. *Nat*  
781 *Methods* 9, 676-682.  
782  
783 Serbus, L.R., Cha, B.J., Theurkauf, W.E., and Saxton, W.M. (2005). Dynein and the actin  
784 cytoskeleton control kinesin-driven cytoplasmic streaming in *Drosophila* oocytes. *Development*  
785 132, 3743-3752.  
786  
787 Tanaka, T., Kato, Y., Matsuda, K., Hanyu-Nakamura, K., and Nakamura, A. (2011). *Drosophila* Mon2  
788 couples Oskar-induced endocytosis with actin remodeling for cortical anchorage of the germ  
789 plasm. *Development* 138, 2523-2532.  
790  
791 Theurkauf, W.E. (1994). Premature microtubule-dependent cytoplasmic streaming in *cappuccino*  
792 and *spire* mutant oocytes. *Science* 265, 2093-2096.  
793  
794 Vig, D.K., Hamby, A.E., and Wolgemuth, C.W. (2016). On the Quantification of Cellular Velocity  
795 Fields. *Biophys J* 110, 1469-1475.  
796  
797 Williams, L.S., Ganguly, S., Loiseau, P., Ng, B.F., and Palacios, I.M. (2014). The auto-inhibitory  
798 domain and ATP-independent microtubule-binding region of Kinesin heavy chain are major  
799 functional domains for transport in the *Drosophila* germline. *Development* 141, 176-186.  
800  
801 Woodhouse, F.G., and Goldstein, R.E. (2013). Cytoplasmic streaming in plant cells emerges  
802 naturally by microfilament self-organization. *Proc Natl Acad Sci U S A* 110, 14132-14137.  
803  
804 Yoo, H., Roth-Johnson, E.A., Bor, B., and Quinlan, M.E. (2015). *Drosophila* Cappuccino alleles  
805 provide insight into formin mechanism and role in oogenesis. *Mol Biol Cell* 26, 1875-1886.  
806  
807 Zimyanin, V.L., Belaya, K., Pecreaux, J., Gilchrist, M.J., Clark, A., Davis, I., and St Johnston, D. (2008).  
808 *In vivo* imaging of *oskar* mRNA transport reveals the mechanism of posterior localization. *Cell* 134,  
809 843-853.  
810

811 **ACKNOWLEDGEMENTS**

812 We are grateful to Dr. Fabio Giavazzi (Milan) for help with the PIV analysis in some of our  
813 experiments. We thank Drs D. St Johnston and I. Davis for reagents, and M. Wayland for  
814 assistance with imaging. We also thank Drs Lena Frerking and Sujoy Ganguly for fruitful  
815 discussions during the initial phase of the project, and Drs MD Martin Bermudo and D. St Johnston  
816 for comments on the manuscript and discussions.

817 MD and IMP were supported by the BBSRC, the University of Cambridge and Queen Mary  
818 University of London. MD was also supported by an Isaac Newton Trust fellowship and  
819 acknowledges funding by the DFG/SFB944 ('Physiology and Dynamics of Cellular  
820 Microcompartments'), the University of Osanbrück and the State of Lower Saxony. LFL and CBS  
821 acknowledge support from the Leverhulme Trust ('Breaking the non-convexity barrier'), EPSRC  
822 (grant No. EP/M00483X/1), the EPSRC Centre (No. EP/N014588/1), the RISE projects CHiPS and  
823 NoMADS, the Cantab Capital Institute for the Mathematics of Information, and the Alan Turing  
824 Institute. LAK was supported by Queen Mary University of London. MB and HD acknowledge  
825 support by the European Research Council (EU FP7-ERC Consolidator Grant No. 615216  
826 LifeInverse). We gratefully acknowledge the support of NVIDIA Corporation with the donation of  
827 the Quadro P6000 GPU used for this research.

828

829 **AUTHOR CONTRIBUTIONS**

830 MD designed and performed research, analyzed data, and wrote the paper. IMP designed  
831 research, analyzed data, and wrote the paper. LAK performed research and analyzed data. LFL  
832 and CBS developed new analytic tools, analyzed the data, and wrote the paper. HD and MB  
833 contributed analytic tools.

834

835 **COMPETING INTERESTS**

836 The authors declare no competing financial interests.

837

838 **DATA AVAILABILITY**

839 The source code of our implementation and of the data analysis is available online  
840 (<https://doi.org/10.5281/zenodo.2573254>). All relevant data and the computational results are  
841 available from the corresponding authors upon request.

## 842 FIGURE LEGENDS

### 843 Figure 1 – MT orientation is aberrant in oocytes with faster flows.

844 **A)** Schematic representation of MT orientation. EB1 specifically associates with the growing end  
845 (plus-end) of MTs and therefore serves as read-out of their spatial orientation. The orientation of  
846 MT growth is represented as an angle, deviating from an imaginary anterior ( $180^\circ$ ) to posterior axis  
847 ( $0^\circ$ ). **B)** Simplified scheme, illustrating the underlying principle of OF-based motion estimation.  
848 Shown are two consecutive frames of a  $5 \times 5$  pixel wide image sequence that contains a  
849 rectangular object of different pixel intensities - from light green (little signal) to dark green  
850 (maximum signal). OF assumes that the intensities of a signal do not change along its trajectory.  
851 Based on this assumption, variational OF allows to estimate a displacement vector for each pixel  
852 (the yellow arrow shows the displacement vector of the centre pixel of the object). **C)** Definition of  
853 growth directions based on OF-estimated velocities. Angles of velocities between  $90^\circ$ - $270^\circ$  are  
854 regarded as anterior (A, blue hemicircle), the complementary set of angles as posterior (P, orange  
855 hemicircle). The sub-population of all posterior signals (orange) that fall between  $330^\circ$ - $30^\circ$  (light  
856 orange sector) are considered to grow towards the 'posterior tip'. **D)** Single frame of an  
857 unprocessed image sequence (raw data) showing an oocyte expressing EB1. The magnified area  
858 is indicated by a dashed box. **E)** Same frame as shown in (D), after applying the denoising step  
859 (Movie S2). Scale bars are  $10 \mu\text{m}$ . **F)** Shown is the OF (displacement vector) field between two  
860 frames of the image sequence in D. **G)** Average OF (over the entire sequence). **H)** Hand-drawn  
861 segmentation mask of the oocyte. For the analysis, only the displacement vectors within this  
862 segmentation were considered. **I)** Staufen (green) localization in control oocytes (arrow). The  
863 protein localizes in a tight posterior crescent by the end of st9. **J)** Living control oocyte expressing  
864 the MT-binding protein Jup (Movie S5). **J')** Kymograph/space-time plot (along the indicated dotted  
865 line in C), showing dynamic bending of MTs over time. **K and M)** Staufen fails to localize in *capu* or  
866 *spire* mutants and distributes throughout the cytoplasm of the cell. **L and N)** Living *capu* (L) or  
867 *spire* (N) mutant oocytes, expressing Jup. Fast cytoplasmic flows lead to the formation of dense  
868 and long MT bundles (red arrows), as well as increased MT bending (Movie S5). **L' and N')**  
869 Kymograph (along dashed line in L and N) indicate a stronger displacement of MT bundles over  
870 time in *capu* (L') or *spire* (N') mutants. **O)** Standard deviation (temporal) projection of EB1 comets  
871 in a control image sequence (in total 65 s). **P)** Rose diagram (angular histogram) with 50 bins  
872 depicting the distribution of EB1 directions in individual control cells within the corresponding  
873 segmented oocyte. Each colour represents the angular histogram of the directions from one  
874 oocyte. **Q)** Same data as shown in (P) with angular histograms averaged over all cells ( $n=8$ ). Error  
875 bars (in black) indicate the standard deviation for each bin (in blue). **R)** Mean angular direction  $\theta_{\text{avg}}$   
876 of the histogram shown in (Q) (also indicated by a red line in (Q)) and the length  $r$  (between 0 and  
877 1) of the mean resultant vector (length of black line in (Q) originating from the centre), which  
878 relates to the circular variance  $S = 1 - r$  of the distribution shown in (Q). Anterior-posterior bias of  
879 all EB1 growth directions. **S)** Rose diagram similar to (P) for control cells but with growth directions



880 binned into four bins (30°-90°, 90°-270°, 270°-330°, and 330°-30°). Moreover, the fraction of  
881 posterior-growing EB1 comets pointing towards the 'posterior tip' (330°-30°) is indicated. **T**  
882 Standard deviation (temporal) projection of EB1 comets in an image sequence of a *capu* mutant  
883 oocyte (in total 65 s). **F-I**) Quantified EB1 directions in *capu* cells, following the same experimental  
884 pipeline described for the control cell.

885

## 886 **Figure 2 – The cytoplasmic actin mesh counteracts the recruitment of Kinesin to MTs**

887 **A,B**) Living control (*capu*<sup>EY12344</sup>/*CyO* in A) and *capu* mutant oocyte (*capu*<sup>EY12344</sup>/*capu*<sup>EY12344</sup> in B),  
888 expressing Khc::GFP. While the fusion protein mainly localizes posteriorly in control cells (A), it  
889 strongly decorates MTs in *capu* mutant cells (B and Movie S10). **C-F**) Fixed control  
890 (*capu*<sup>EY12344</sup>/*CyO*) oocytes (C,D) and *capu* mutant cells (*capu*<sup>EY12344</sup>/*capu*<sup>EY12344</sup>) (E,F), expressing  
891 Khc::GFP. Cells were stained against  $\alpha$ Tubulin (magenta) and the Kin1-700-GFP fusion protein  
892 (green). In controls, Tubulin and Khc::GFP localize to opposed gradients and show little overlap  
893 (C,D). Conversely, in *capu* mutants, Khc::GFP strongly co-localizes with Tubulin (red arrows in  
894 E,F). Insets in D and F show merged channels. **G-L**) Higher resolution images of fixed control  
895 (*capu*<sup>EY12344</sup>/*CyO*) (G-I) and *capu* mutant (J-L) cells, stained against  $\alpha$ Tubulin (magenta) and GFP  
896 (green). While Khc::GFP localizes diffusely around MTs in control cells (G-I), it strongly co-  
897 localizes to MTs in *capu* mutants (red arrows in J-L). **M-P**) The cytoplasmic actin mesh in control  
898 (M, *capu*<sup>EY12344</sup>/*CyO*) and transheterozygous *capu*<sup>EY12344</sup>/*capu*<sup>L219</sup> (N), *capu*<sup>EY12344</sup>/*capu*<sup>L201</sup> (O), and  
899 *capu*<sup>EY12344</sup>/*capu*<sup>38</sup> (P). **Q**) Quantification of signal intensities of the actin mesh as shown in (M-P). All  
900 cells harbor the strong hypomorphic allele *capu*<sup>EY12344</sup> over either *CyO* (n=15), *capu*<sup>L219</sup> (n=21),  
901 *capu*<sup>L201</sup> (n=20) or *capu*<sup>38</sup> (n=21). **R-T**) Khc::GFP expressed in living *capu*<sup>EY12344</sup>/*capu*<sup>L219</sup> (R),  
902 *capu*<sup>EY12344</sup>/*capu*<sup>L201</sup> (S), and *capu*<sup>EY12344</sup>/*capu*<sup>38</sup> (T) oocytes. Red arrows indicate Khc::GFP positive  
903 MT bundles.

904

## 905 **Figure 3 – Kin activity impacts on the spatial orientation of MTs in the oocyte.**

906 **A-C**) Still frames and kymographs of live oocytes expressing Jup. Cells harbor a null mutation  
907 (*khc*<sup>null</sup> (27)), or single point mutations in the motor domain (*khc*<sup>slow</sup> (23) and *khc*<sup>slow</sup> (17)), rendering  
908 the motor slower. Compared to controls, all *khc* mutant cells exhibit no cytoplasmic flows and thus  
909 no MT bulk motion (Movie S6). **D-F**) Posterior cargo localization in different *khc* mutant alleles.  
910 Staufen (green) is not transported to the posterior in cells lacking Kin (*khc*<sup>null</sup> (27)) and is found in  
911 the anterior corners of the cell (arrows). In contrast, in both of the slow Kin alleles (*khc*<sup>slow</sup> (23) and  
912 *khc*<sup>slow</sup> (17)) a considerable amount of Staufen becomes transported to the posterior. However,  
913 compared to controls (Figure 2A) Staufen is not only localized in a posterior crescent, but also in  
914 dots within the posterior cytoplasm (arrows). **G-P**) OF analysis of EB1 growth directionality in  
915 *khc*<sup>slow</sup> (G-K, n=10) and *khc*<sup>null</sup> (L-P, n=10) oocytes, following the same experimental pipeline  
916 described in Figure 1.

917

918

919 **Figure 4 – Anterior and posterior regional impact of Kin activity on MT orientation.**

920 **A)** Single frame of an oocyte expressing EB1. Dashed lines represent the anterior and posterior  
921 regions of the oocyte used to extract orientation data. **B)** Global EB1 signal directions within the  
922 entire oocyte (as shown in Figure 1 and 3). **C-H)** In each case, from left to right: distribution of EB1  
923 growth orientation visualized in a rose diagram, the anterior-posterior orientation, and the ‘posterior  
924 tip’ orientation. **C,D)** Data for control cells (n=8). **E,F)** Data for *khc<sup>slow</sup>* mutant cells (n=10). **G,H)**  
925 Data for *khc<sup>null</sup>* mutant cells (n=10).

926

927 **Figure 5 – Cytoplasmic streaming constitutes a major contributor to MT orientation.**

928 **A,B)** Posterior cargo localization in *capu,khc<sup>slow</sup>/+* (A) and *capu,khc<sup>slow</sup>* double (B) mutant cells.  
929 While Staufen (green) partially localizes to the posterior of the cell in *capu,khc<sup>slow</sup>/+* oocytes (right  
930 arrow in A), the majority of the protein localizes in cytoplasmic clouds (left arrow in A). In  
931 *capu,khc<sup>slow</sup>* double mutant cells, Staufen localizes in a posterior crescent but also accumulates in  
932 dots close to the posterior (arrow in B). **C,D)** Still frames and kymographs of live *capu,khc<sup>slow</sup>/+*  
933 (C,C’) or *capu,khc<sup>slow</sup>* double (D,D’) mutant oocytes, expressing Jup. **E-N)** OF analysis of EB1  
934 growth directionality in *capu,khc<sup>slow</sup>/+* (E-I, n=10) and *capu,khc<sup>slow</sup>* (J-N, n=8) oocytes.

935 TABLES

936

937

Table 1 – Summary of EB1 orientation data, extracted from confocal time series by variational OF analysis.

genotype	n	global EB1::GFP					EB1::GFP in anterior oocyte			EB1::GFP in posterior oocyte		
		% ant.	% post.	% post. tip	$\theta_{avg}$	r	% ant.	% post.	% post. tip	% ant.	% post.	% post. tip
control	8	34 ± 6	66 ± 6	40 ± 4	353.08±0.05	0.260	38 ± 5	62 ± 5	40 ± 5	26 ± 11	74 ± 11	41 ± 8
capu	10	39 ± 14	61 ± 14	25 ± 8	318.92±0.06	0.182						
khc <sup>null</sup>	10	38 ± 6	62 ± 6	41 ± 7	357.35±0.07	0.202	44 ± 4	56 ± 4	36 ± 3	28 ± 13	72 ± 13	46 ± 13
khc <sup>slow</sup>	10	25 ± 10	75 ± 10	54 ± 15	1.62±0.02	0.412	26 ± 11	74 ± 11	52 ± 14	19 ± 10	81 ± 10	57 ± 17
capu,khc <sup>slow</sup> +	10	39 ± 13	61 ± 13	34 ± 5	335.08±0.07	0.167						
capu,khc <sup>slow</sup>	8	34 ± 15	66 ± 15	39 ± 5	19.67±0.05	0.285						
<b>Tracking data from Parton et al. 2011</b>												
control		42	58				46	54		37	63	
par-1		49	51									

	similar to control
	stronger posterior bias
	weaker posterior bias

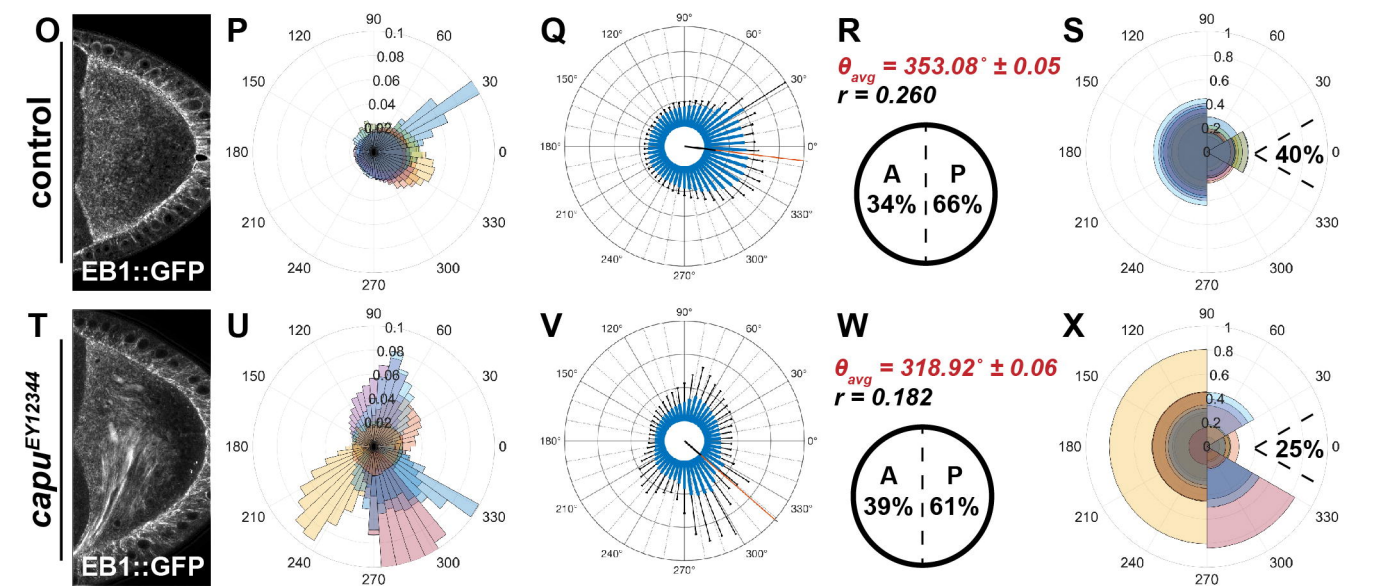
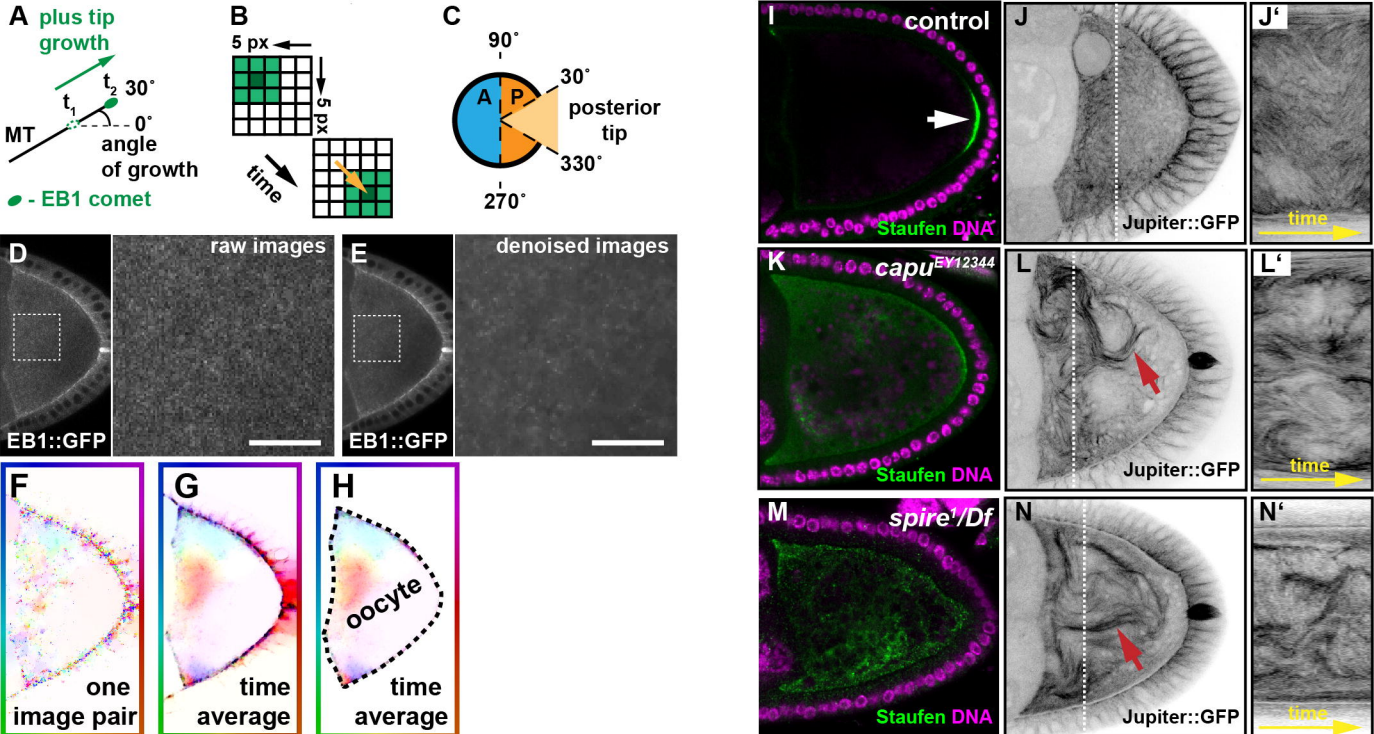
938

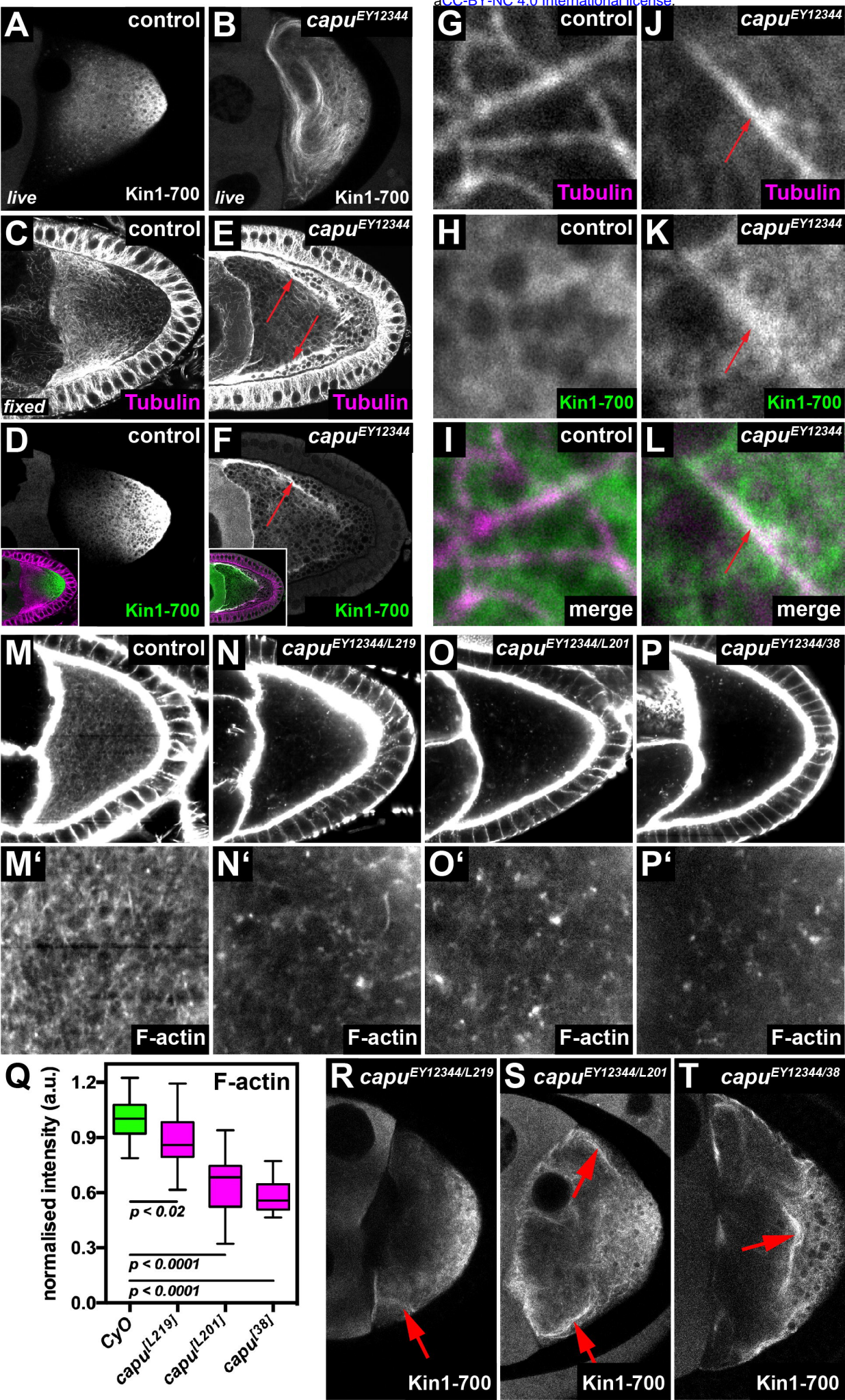
939

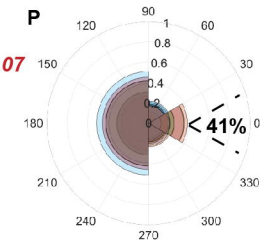
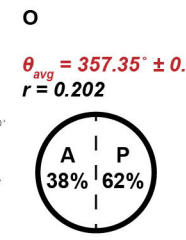
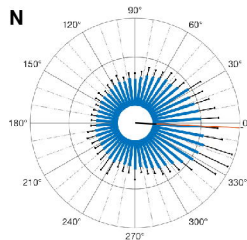
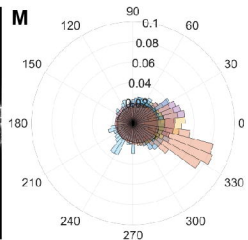
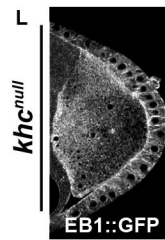
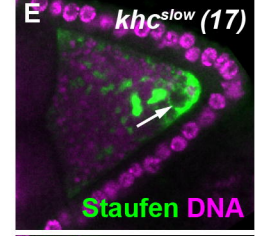
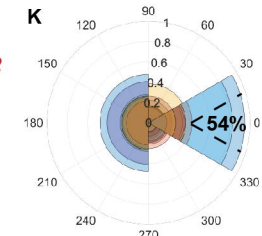
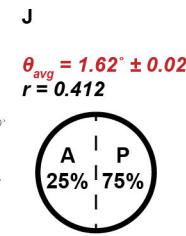
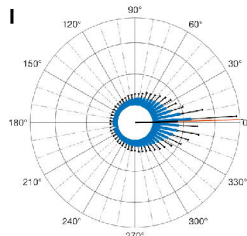
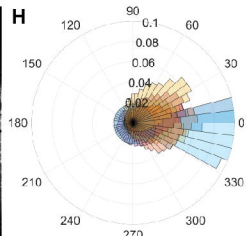
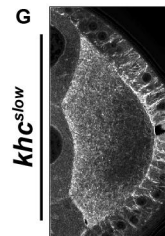
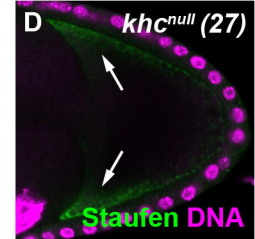
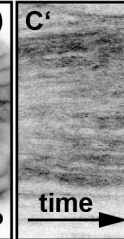
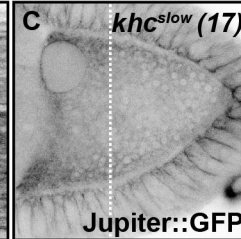
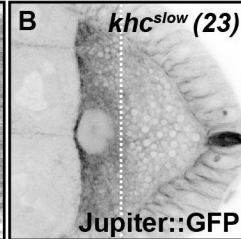
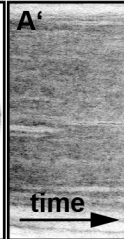
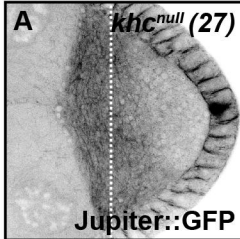
940

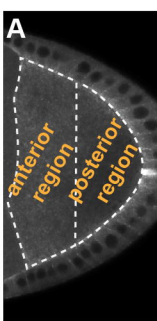
941

Anterior-posterior orientation bias of microtubule growth in per cent ( $\pm$  95% confidence interval).  $n$  represents the number of cells analyzed.  $\theta_{avg}$  gives the average angle of all EB1 orientations of all cells of a given genotype.  $r$  constitutes a measure of variance and lies between 0 and 1. The larger  $r$ , the less variable the data set.









**B** global EB1

